Accepted Manuscript

Birth of an ocean in the Red Sea: Oceanic-type basaltic melt intrusions precede continental rupture

Marco Ligi, Enrico Bonatti, William Bosworth, Yue Cai, Anna Cipriani, Camilla Palmiotto, Sara Ronca, Monique Seyler

PII: S1342-937X(17)30331-3
DOI: doi:10.1016/j.gr.2017.11.002
Reference: GR 1877

To appear in:

Received date: 4 August 2017
Revised date: 12 October 2017
Accepted date: 1 November 2017

Please cite this article as: Marco Ligi, Enrico Bonatti, William Bosworth, Yue Cai, Anna Cipriani, Camilla Palmiotto, Sara Ronca, Monique Seyler , Birth of an ocean in the Red Sea: Oceanic-type basaltic melt intrusions precede continental rupture. The address for the corresponding author was captured as affiliation for all authors. Please check if appropriate. Gr(2017), doi:10.1016/j.gr.2017.11.002

Birth of an Ocean in the Red Sea: Oceanic-type Basaltic Melt Intrusions Precede Continental Rupture

Marco Ligi[a,*], Enrico Bonatti[a,b], William Bosworth[c], Yue Cai[b], Anna Cipriani[b,d], Camilla Palmiotto[a], Sara Ronca[e], Monique Seyler[f]

[a] *Istituto di Scienze Marine, CNR, Via Gobetti 101, 40129 Bologna, Italy.*

[b] *Lamont Doherty Earth Observatory of Columbia University, 61 Route 9W, Palisades, New York 10964, USA.*

[c] *Apache Egypt Companies, New Maadi, Cairo, Egypt.*

[d] *Dipartimento di Scienze Chimiche e Geologiche, Universita` degli Studi di Modena e Reggio Emilia, Via Campi 103, 41100 Modena, Italy.*

[e] *Dipartimento di Scienze della Terra, La Sapienza Universita` di Roma, P. Aldo Moro 5, 00185 Rome, Italy.*

[f] *Laboratoire d'Océanologie et de Géosciences, UMR LOG 8187 CNRS-Lille1-ULCO, UFR Sciences de la Terre - Bât. SN5, F59655 Villeneuve d'Ascq, France.*

*Corresponding author: marco.ligi@bo.ismar.cnr.it.

Abstract

The role of magmatism in continental rupture at the birth of a new ocean is poorly understood. Continental rupture can take place with voluminous volcanism, as in the southern Red Sea, or in a relatively non-volcanic mode, as in the northern Red Sea. We report geophysical, geochemical and geochronological evidence suggesting that continental rupture in the northern Red Sea is preceded by MORB-type basaltic melt intrusions that cooled at depth forming gabbros at progressively shallower crustal levels as rifting progressed towards continental separation. One of these gabbros yielded an $^{40}Ar/^{39}Ar$ age of 25±6 Ma, suggesting intrusion during early rifting. A magma chamber we detected 3.5 km below Thetis Deep, an axial segment of initial oceanic crust accretion, represents the final stage in this progression. Oceanic crust accretion in the Red Sea rift starts first at depth before continental rupture and initiation of sea floor spreading.

Research highlights

Northern Red Sea is floored by continental crust with a few basaltic injection sites

New constraints on composition, depth and age of syn-rift magma intrusions are given

Oceanic melt emplacement in narrow rift starts at depth during continental rifting

Keywords: rifting; magmatic intrusions; continental rupture; seafloor spreading initiation; northern Red Sea.

1. Introduction

As hinted already by Alfred Wegener over 80 years ago (Wegener, 1929), the Red Sea provides today the prime example of a rupturing continent, with Arabia separating from Africa, and a new ocean being born in between. Axial accretion of oceanic crust accompanied by Vine-Matthews magnetic anomalies started roughly 5 Ma in the southern Red Sea, and 3 to 1 Ma in discrete axial cells within the central Red Sea (Fig. 1), in a pattern suggesting northward propagation of the nascent oceanic rift (Girdler and Styles, 1974; Bonatti, 1985; Ghebreab, 1998; Cochran, 2005; Bosworth et al., 2005; Ligi et al., 2012). As far as the northern Red Sea, north of the Zabargad Shear Zone, some authors favour prevalence of oceanic crust (LaBrecque and Zitellini, 1985; Girdler, 1985; Gaulier et al., 1988; Sultan et al., 1992, Dyment et al., 2013; Tapponier et al., 2013), others prevalence of thinned and stretched continental crust (Cochran, 1983; Bonatti, 1985; Cochran and Martinez, 1988; Guennoc et al., 1988; Bosworth, 1993; Ghebreab, 1998; Cochran, 2005; Bosworth et al., 2005; Mitchell and Park, 2014; Almalki et al., 2015; 2016). No borehole data are available as to the nature of the crust beneath the main trough. Gravity and magnetic data can be interpreted as due to either continental or oceanic sources; however, the tectonic style of the basement is hidden by a thick, high-velocity evaporitic layer, that reduces penetration in multichannel seismic reflection profiles and masks data potentially useful to clarify its origin (Mitchell et al., 2017).

We present here 3D seismic reflection and gravity data obtained from an off-axis area of the NW Red Sea (Fig. 1), as well as a study of gabbroic rocks recovered in the same area both from an oil well (QUSEIR B-1X) below a thick syn-rift sediment pile, and from a layered mafic complex exposed on the Brothers islands (Fig. 2). These gabbros show geochemical signatures similar to those of mid-ocean ridge basalts (MORB) (Fig. 3). Our results suggest that the northern Red Sea is carpeted by stretched and thinned continental crust injected by MORB-type intrusions. In addition, we detected a magma chamber beneath Thetis Deep, an axial cell of initial oceanic crust formation (Fig. 4). These new data suggest progressively shallower intrusions of MORB-type melts during rifting, implying that “oceanization” in the northern Red Sea occurred first at depth, preceding

continental rupture and sea floor spreading.

2. Data and Methods

2.1 Multibeam bathymetry

Bathymetry was acquired during a 2005 R/V Urania (RS05) cruise (Mitchell et al., 2010; Ligi et al., 2011) with a RESON SeaBat 8160 multibeam, DGPS positioning, and TSS MAHRS MRU and gyrocompass. Data processed by the Kongsberg Neptune package produced Digital Terrain Models with up to 25 m of grid resolution. Topography of the northern Red Sea was obtained from a synthesis of our own multibeam and single-beam data (Bonatti et al., 1984) acquired in 1979 (R/V Salernum, MR79) and 1983 (R/V Bannock, MR83); multibeam data (Cochran and Martinez, 1988; Guennoc et al., 1988; Haase et al., 2000) from cruises MEROU (R/V Charcot, 1978), RC2507 (R/V Conrad, 1984) and M31L2 (R/V Meteor, 1995); plus water depth data obtained by converting to depth the two-way travel time of the 3D seismic seafloor reflector using a constant velocity of 1525 m/s; bathymetric grids from GEBCO and NGDC databases (https://www.bodc.ac.uk/data/; http://www.ngdc.noaa.gov/mgg/); and elevation data from the Shuttle Radar Topography Mission (SRTM) database (http://srtm.usgs.gov/). Spatial analysis and mapping were performed using the PLOTMAP package (Ligi and Bortoluzzi, 1989).

2.2 Gravity

Shipboard gravity measurements from NGDC database, were corrected with the techniques outlined in Ligi et al. (2012) and combined with satellite-derived free-air gravity data (Sandwell et al., 2014; version 23.1) in order to add the ship-gravity high-frequency content to the full coverage of satellite data. Bouguer anomalies were obtained by subtracting from the free air anomalies the attraction of seafloor topography (Fig. 5). The zero level of the Bouguer anomalies is arbitrary and corresponds to the center of the range in anomaly amplitudes (Fig. 5).

2.3 Seismic reflection

Details on acquisition parameters and processing flow of multichannel seismic reflection data acquired during the 2005 R/V Urania (RS05) cruise can be found in Ligi et al. (2012).

The block of 3D seismic reflection data from offshore Egypt (Fig. 1) was acquired in 1999 for BG (Gordon et al., 2010). A few details of acquisition and processing methods are available to us. The time migrated reflection profiles from the 3D seismic survey were included into the seismic and geological interpretation software IHS *Kingdom*® in order to map the top and the base of major tectonic sequences, such as the top of evaporites, the base of evaporites, the rift-onset unconformity and the top of igneous basement.

2.4 Elemental chemistry

Whole rock major and trace element composition of the Brothers rocks were obtained by lithium metaborate/tetraborate fusion ICP-AES and ICP–MS, at Activation laboratories Inc. (Ontario, Canada) according to Code 4Lithoresearch package, and by ICP-OES (Agilent 720) at Lamont-Doherty Earth Observatory of Columbia University (LDEO) on solutions prepared with lithium metaborate fusion. FeO was determined by redox titration ($KMnO_4$ titration). Loss On Ignition (LOI) was measured according to standard gravimetric procedure and corrected for Fe oxidation.

Mineral composition of the Brothers and QUSEIR gabbros were determined using an automated CAMECA SX50 microprobe operating in full WDS mode at the University of Rome La Sapienza (IGAG - Istituto di Geologia Ambientale e Geoingegneria). An acceleration potential of 15 kV with a sample current of 15 nA (measured on brass) was applied. The beam size was varied as a function of the analyzed phase. Natural and synthetic oxides and silicates were used as standards. Samples and standards were carbon coated. On-line corrections for drift, dead-time and background were applied to the raw data.

In-situ trace elements have been measured at the Centro Interdipartimentale Grandi Strumenti (CIGS) of the Università of Modena and Reggio Emilia using a Nd:YAG deep UV (213 nm) New Wave Research UP-213 laser ablation system (LA) coupled to a Thermo Fisher Scientific X-Series II Induced Coupled Plasma Mass Spectrometer (ICP-MS). Instrumental drift correction was computed by linear correction of measured intensities among repeated measurements of the NIST 610, 612 and 614 glasses with ^{44}Ca as the internal standard. Analytical routine includes 100 μm pre-

ablation scan (dwelling time: 2 s, 5 Hz laser fire, laser fluency 18÷20 J/cm^2) followed by 80 μm ablation scan (dwelling time: 30 s, 20 Hz laser fire, laser fluency 18÷20 J/cm^2). Data reduction performed with Plasma Lab® software by Thermo Scientific. Precision and accuracy, both better than 10% for concentrations at the ppm level, were assessed from repeated analyses of NIST 610, 612 and 614 standards.

2.5 Geothermometry and Geobarometry

Pressure conditions during crystallisation were estimated using the cpx geobarometers of Nimis and Ulmer (1998) and Nimis (1999) based on the cpx structural parameters calculated from major-element composition. The cpx geobarometer is calibrated for different magma compositions. TH (tholeiitic series) calibration was used for Brothers and QUSEIR gabbros whereas MA (mildly alkaline series) calibration was used for Zabargad rocks. Equilibration temperatures of the cumulate rocks were estimated by means of various geothermometers: olivine-augite geothermometer based on Fe-Mg exchange (Loucks 1996), applicable to mineral assemblages including ol+pl+cpx±opx or pigeonite; two-pyroxene geothermometer (Frost and Lindsley, 1992) in the QUILF program (Andersen et al., 1993); pyroxene thermometer for cpx +opx intercumulus assemblages; projection of the pyroxene compositions onto Lindsley's isotherms (Lindsley, 1983) providing minimum equilibration temperature for cpx; Ti-in-amphibole geothermometer (Ernst and Liu, 1998) using calibrated values (Femenias et al., 2006) in order to estimate crystallization temperatures of interstitial magmatic, late-magmatic and subsolidus amphiboles.

2.6 Isotope chemistry

Nd, Sr and Pb, isotope ratios of QUSEIR and Brothers gabbros were measured on whole rock powders and mineral separates. Mineral separates were carefully checked under a binocular microscope to avoid any inclusion or alteration. Minerals and powders were strongly leached with a solution of 6.2N HCl and 5% HF. Pb was separated using AG1-X8 anion resin, Sr was separated using Eichrom Sr resin and Nd was separated in a two-column procedure using Eichrom TRU-spec resin to separate the REE, followed by alfa-hydroxy isobutyric acid. The Sr, Nd and Pb isotopic

compositions were measured on a VG Sector 54 multicollector thermal ionization mass spectrometer at Lamont Doherty Earth Observatory of Columbia University. The $^{143}Nd/^{144}Nd$ and $^{87}Sr/^{86}Sr$ ratios were normalized to an $^{86}Sr/^{88}Sr$ ratio of 0.1194 and $^{146}Nd/^{144}Nd$ ratio of 0.7219, respectively, and reported relative to the La Jolla Nd standard $^{143}Nd/^{144}Nd = 0.511860$ and NBS987 $^{87}Sr/^{86}Sr = 0.710248$. Samples and duplicates were analyzed during two analytical sessions. Repeated measurements of the NBS987 Sr standard during the 2 sessions yielded $^{87}Sr/^{86}Sr$ of 0.710272 ± 0.000011 (2σ, N = 7, 16 ppm external reproducibility) and of 0.710261 ± 0.000020 (2σ, N = 13, 28 ppm). Repeated measurements of the Nd La Jolla and JNdi-1 standards during the two sessions yielded $^{143}Nd/^{144}Nd$ of 0.511844 ± 0.000020 (2σ, N = 9, 40 ppm external reproducibility) and of 0.512078 ± 0.000016 (2σ, N = 7, 32 ppm), respectively.

Lead isotopes data were collected in static mode using a $^{207}Pb/^{204}Pb$ double spike. The measurements of unspiked–double-spiked pairs of the NBS 981 standard were replicated to 179, 233 and 296 ppm (2-s.d. external reproducibility, n = 39) for $^{206}Pb/^{204}Pb$, $^{207}Pb/^{204}Pb$ and $^{208}Pb/^{204}Pb$ ratios, respectively. Measured Pb isotope ratios were corrected to values of 16.9356, 15.4891, and 36.7006, respectively, for NBS 981 (Todt et al., 1996).

2.7 $^{40}Ar/^{39}Ar$ dating

A fragment of QUSEIR gabbro was crushed and sieved. Plagioclase crystals were separated from the 60-150 mm size fraction using a magnetic separator; the cleanest crystals were hand-picked under a microscope. Sample was co-irradiated with Fish Canyon sanidine (dated at 28.201 ± 0.046 Ma) at the USGS TRIGA reactor in Denver, CO, US. The irradiated sample was placed in Ta tubes, and evacuated in a chamber with glass window for incremental heating with a diode laser (PhotonMachines). Stepwise heating of the sample was conducted with energies of 1 to 18 W. Released argon was cleaned of active gasses by interaction with Zr-Al getters set at 2 amps, and then allowed into the WG5400 noble gas mass spectrometer for analyses using peak-hopping on an analogue multiplier. Argon data were corrected for backgrounds and discrimination using frequently measured blanks and air pipettes. Corrections were made for nuclear interferences using the information from Dalrymple et al. (1981) for the USGS reactor. The J-values were calculated

from the average of Fish Canyon sanidines that were co-irradiated with the sample, for a given irradiation level.

3. Results

3.1 Extensional Tectonics and gabbro intrusions in the Northern Red Sea

The Zabargad Shear Zone (SZ), a topographic feature running NNE-SSW across the entire width of the Red Sea roughly parallel to the Dead Sea Fault, offsets the Red Sea axis by ~100 km and marks the southern limit of the northern Red Sea (Fig. 1). The Zabargad SZ acts as a transfer zone joining two axial rift segments and accommodating extension through a strike slip fault system (Crane and Bonatti, 1987). It can be considered a precursor to a future oceanic fracture zone. North of the Zabargad SZ and along the main trough of the Red Sea (Fig. 1), the only deeps clearly floored by MORB-type basalts are Mabahiss and Shaban (Guennoc et al., 1988; Haase et al., 2000). Mabahiss Deep lies at the NE end of the Zabargad SZ and has been interpreted as a pull-apart basin (Guennoc et al., 1988). North of Mabahiss, the only area where recent continental rupture can be inferred is at Shaban Deep, located along the main trough ~40 km east of Brothers Islands (Fig. 1). In the center of the Deep an elongated NW-SE 6 km-long volcanic ridge (Ehrhardt and Hubscher, 2015) exposes basaltic glasses that derive from a depleted mantle source (MORB source) with no contamination by continental lithosphere (Haase et al., 2000), similarly to glasses from the axial zone of Thetis and Nereus in the northern sector of the central Red Sea (Ligi et al., 2012; 2015). Differences both in major elements (higher Na_2O, lower FeO_T in Shaban compared to Nereus/Thetis lavas) and in incompatible elements (higher La/Sm in Shaban than in Nereus/Thetis basalts) indicate that the degree of melting decreases from south to north along the Red Sea rift and melting occurs at progressively shallower depths with northern magmas generated from a relatively cold shallow mantle (Haase et al., 2000; Ligi et al., 2012).

We interpreted a 3D seismic reflection survey of an area west of Shaban Deep, in the African side of the northern Red Sea (Gordon et al., 2010) (Figs 1 and 2), where the summit of a NW-SE elongated uplifted crustal block emerges in the two small Brothers islands (Fig. 2), that

expose gabbroic rocks cut by doleritic dykes below a thin Pleistocene carbonate cap (Shukri, 1944; Hoang and Taviani, 1991; Bonatti and Seyler, 1987). The Brothers are part of a series of sub-parallel topographic highs associated with right lateral transtension, including to the southwest a prominent NW-striking SW-dipping extensional fault block (Fig. 2). Few kilometres east of the Brothers, an WSW-ENE elongated transtensional depression (Oceanographer Deep) lies at the intersection of a left-stepping transcurrent fault parallel to the Dead Sea transform and a NE right-stepping transcurrent fault normal to the present rift axis (Fig. 2).

Gabbros were also sampled beneath a ~4 km thick sedimentary sequence, dominated by evaporites, at the base of the QUSEIR B-1X (QUSEIR) drill hole, ~80 km south of the Brothers (Fig. 1). A strong reflector we mapped beneath the Miocene evaporites can be interpreted as the top of the crystalline basement (Fig. 2). Bouguer gravity data suggest that it marks the top of the same gabbro unit sampled in the QUSEIR drill hole and on the Brothers (Fig. 5). Gabbros are found also on Zabargad Island, a block of sub-Red Sea lithosphere uplifted by transpression (Crane and Bonatti, 1987) at the SW end of the Zabargad SZ (Fig. 1). Zabargad exposes also mantle-derived peridotite bodies and Pan African silicic gneisses intruded by doleritic dykes (Bonatti and Seyler, 1987; Bonatti et al., 1986).

We discuss next the nature of the Brothers, QUSEIR and Zabargad gabbros and their role in the opening of the northern Red Sea.

3.2 Brothers and QUSEIR gabbros

Textures, petrology and geochemistry of the Brothers gabbros indicate that they are part of a layered cumulitic complex including leucotroctolites, olivine gabbros, and anorthositic gabbros crosscut by amphibole-bearing olivine microgabbronorites. The QUSEIR borehole sample is a medium to coarse-grained olivine leucogabbro with mesocumulate texture and no foliations, igneous laminations, or magmatic layering. Primary phases are variably affected by hydrothermal alteration ranging from high-temperature amphibolite facies (near-solidus) to low temperature facies. Cpx REE patterns exhibit depleted LREE and flat HREE, similar to those of calculated cpx in equilibrium with N-MORB (Fig. 3 and Tab. 1). Overall, bulk rock major, trace element and

mineral chemistry of Brothers and QUSEIR gabbros resemble those of cumulates from mid-ocean ridges.

Nd isotope ratios of the Brothers and QUSEIR gabbros and their mineral separates plot within the field of Red Sea "true" oceanic crust and global MORB (Fig. 3). Their high Sr isotope ratios at relatively constant Nd isotope ratios probably result from hydrothermal alteration. Cpx, plg and bulk data of QUSEIR gabbros define a pseudo-isochron of about 20 Ma. Given the cpx alteration, this age could indicate a metamorphic age of the gabbros due to reaction with seawater. They have slightly more "enriched" isotopic compositions than average MORB, possibly reflecting the influence of the Afar plume (Deniel et al., 1994) (Fig. 3 and Tab. 2). In a plot of $^{207}Pb/^{204}Pb$ versus $^{206}Pb/^{204}Pb$ most Brothers samples fall next to the Afar plume field, slightly above the NHRL, but close to the values for the Red Sea region (Volker and McCulloch, 1993). In a $^{208}Pb/^{204}Pb$ versus $^{206}Pb/^{204}Pb$ plot the samples lie within a trend explained by binary mixing between a depleted and an enriched mantle component. The presence of an ancient incompatible element enriched component in the source of the Brothers gabbros supports the idea of a long-term influence of the Afar plume in the Red Sea region (Volker and McCulloch, 1993).

We obtained $^{40}Ar/^{39}Ar$ ages of plagioclase crystals separated from a sample of the QUSEIR gabbro using a step heating method. The Ar content of the plagioclase is low, and the $^{40}Ar/^{39}Ar$ ages derived from all the heating steps all fall within each other's error, yielding a plateau age of 25 ± 6 Ma (n=10). These steps fall on an isochron with a younger age of 16 ± 7 Ma and an initial $^{40}Ar/^{36}Ar$ value of 305 ± 4 that is similar to that of air. The two ages overlap within error (Fig. 6). These ages are consistent with the Sm-Nd pseudo-isochron age of 20 Ma.

Metagabbros outcropping on Zabargad island have an olivine alkali basalt composition (Bonatti and Seyler, 1987; Seyler and Bonatti, 1988), different from the MORB-type composition of Brothers and QUSEIR gabbros. As consequence of strong alteration, dating of the Zabargad mafic rocks gave an unreasonably broad range of ages (Nicolas et al., 1985; Villa, 1990; Bosworth et al., 1996) and are clearly not indicative of the timing of intrusions unless a very prolonged

intrusion history is envisioned, that is not supported by field relationship (Bosworth and Stockli, 2016).

Pressures of crystallization estimated from cpx geobarometry (Nimis and Ulmer, 1998; Nimis, 1999) are 2.8+/-0.12 kbar and 3.0+/-0.26 kbar for Brothers and QUSEIR gabbros, respectively. These pressures correspond to 10-13 km depth assuming crustal density of 2670 kg/m^3. The ^{VI}Al/^{IV}Al ratios of cpx (Aoki and Kushiro, 1968) confirm a shallow intrusion crystallization for Brothers and QUSEIR gabbros, comparable to that of the SW Indian Ridge gabbros (Hebert et al., 1991).

In contrast, geobarometry on primary cpx from the Zabargad pyroxenite-gabbro complex with alkaline affinity yields pressures as high as 8-9 kbar, in agreement with pressures estimated from mineral associations and composition (Seyler and Bonatti, 1988). These data suggest crystallization at a depth of ~30-35 km, followed by retrograde metamorphism under decreasing pressure conditions, probably due to uplift in the presence of fluids (Bonatti and Selyer, 1987; Seyler and Bonatti, 1988). Given that uplift occurred probably close in time to crystallization of the gabbros (Seyler and Bonatti, 1988), the Zabargad gabbros probably intruded the base of the continental crust during the initial stages of rifting. In summary, the Brothers and QUSEIR gabbros crystallized probably at relatively shallow depths (~10-13 km) from melts derived from early fractionation of a MORB-type primary magma, while the Zabargad gabbros derive instead from an alkali basalt magma that crystallized significantly deeper (30-35 km).

3.3 Red Sea sub-axial magma chamber

The two northernmost axial segments of oceanic crust accretion in the central Red Sea, known as Nereus and Thetis Deeps (Fig. 1), are carpeted by fresh oceanic basalts that rose from an asthenospheric source uncontaminated by continental components in the initial stages of continental break up (Ligi et al., 2011; 2012). Thetis Deep formed by the coalescence of three rift valley sub-segments, each with an axial neovolcanic zone. Magnetic anomalies constrain the initial oceanic accretion at about 2.2 Ma in the southern and older sub-segment (Ligi et al., 2012). Seismic reflection profile TL-23M (Fig. 4), obtained across the Thetis southern sub-segment, shows a ~5 km

wide reflector ~1.4 seconds below the axial neovolcanic zone, with polarity opposite to that of the seafloor reflector (Fig. 4). This reflector marks the roof of a magma chamber or melt lens, similar to those identified below mid-ocean ridges (Detrick et al., 1987; Singh et al., 2006). Assuming a 4.5 km/s acoustic velocity for the upper oceanic crust at Thetis (Tramontini and Davis, 1969), this reflector is located ~3.2 km below the seafloor, implying that the top of the alleged magma chamber lies deeper than most of those identified below Mid Ocean Ridges, supporting the idea that the depth of sub-ridge magma chambers is inversely proportional to spreading rate (Purdy et al., 1992). The Thetis magma chamber upon cooling is likely to produce gabbroic rocks similar to those of Brothers and QUSEIR, except for their lower crystallization pressure.

4. Discussion

4.1 Nature of crust in the northern Red Sea

Petrologic and geochemical data of the QUSEIR and Brothers gabbros are compatible with their having been emplaced either in a continental or in an oceanic context, renewing the controversy on the nature of the crust in the northern/central Red Sea, i.e., the crust outside the axial oceanic cells is either oceanic or it consists of melt-intruded extended continental crust.

The lack of organised magnetic anomalies North of the Zabargad FZ where the coasts are straight (Cochran, 2005); the seismicity scattered across the basin (Hosny et al., 2013), the high-density crustal layers just beneath evaporites (El-Bohoty et al., 2012); the low seismic velocity gradients (Gaulier et al., 1988); and the presence of Precambrian shield rocks in boreholes near the coasts (Bosworth, 1993; Almalki et al., 2015), all support the idea that the northern Red Sea is carpeted by stretched and thinned continental crust (Fig. 7), with a few isolated sites of basaltic injection (Cochran, 1983; Bonatti, 1985; Cochran and Martinez, 1988; Guennoc et al., 1988; Bosworth, 1993; Cochran, 2005; Mitchell and Park, 2014).

Based on their $^{40}Ar/^{39}Ar$ ages the QUSEIR gabbros cannot be part of the Pan-African continental lithosphere. It is also unlikely that they were emplaced during an hypothetical current episode of seafloor spreading, as the age of the oceanic crust at the QUSEIR site would be not older than 10-12 Ma (assuming continuous seafloor spreading and the 8-9 mm/a present day plate

separation (Chu and Gordon, 1998). Instead these ages are consistent with the hypothesis that QUSEIR gabbros intruded thinned and stretched continental crust during early Red Sea rifting. Assuming stretching starts at 25 Ma, then 5 Ma of rifting at 10 mm/a is expected to result in 50 km of extension. Given a pre-rift rift width of 50 km then 5 Ma of extension causes doubling the rift width to 100 km. Assuming uniform extension and that the pre-rift crustal thickness is 30 km along with little extension by intrusion, results in a predicted crustal thickness of 15 km (i.e., stretching factor of 2) for the Red sea at 20 Ma. Our 10-13 km depth of emplacement is therefore consistent with intrusion into the lower crust. This implies that the Brothers and QUSEIR gabbros were intruded into sub-rift continental crust and then exhumed by footwall-uplift during extension and block rotation, in a mechanism similar to that proposed for the basement cores of oceanic core complexes and/or of fault blocks exposed in the Gulf of Suez (Bosworth et al., 2005).

4.2 A rifting model for the northern Red Sea

The Zabargad pre-rift high-P gabbros, the QUSEIR and Brothers pre-break-up low-P gabbros, and the Thetis post-break-up subaxial "oceanic" magma chamber can be interpreted as steps in a sequence of progressively shallower melt intrusions from alkali basalt to MORB as rifting progressed in the northern Red Sea towards continental rupture and initial sea floor spreading (Fig. 8). The 22 Ma Jabal Tirf gabbros, part of the Miocene Tihama Asir intrusive complex located along the southern Red Sea coast of Saudi Arabia (McGuire and Coleman, 1986) may also represent pre-break up shallow basaltic intrusions, similar to the QUSEIR and Brothers intrusions. Zabargad gabbros crystallized deeper and may represent alkali-basalt melt injected at the base of the continental crust before and during the very early stages of rifting. The QUSEIR and Brothers gabbros indicate that oceanic-type basaltic melts generated by the pre-opening subrift mantle can be emplaced at depth without erupting on the seafloor. In line with this model, initial melts producing the earliest Vine-Matthews stripes at the Thetis and Nereus "oceanic" segments have a MORB composition with no significant contamination from continental lithosphere (Ligi et al., 2012). The presence of a few kilometers deep subrift magma chamber soon after the initiation of oceanic spreading implies crystallization of lower oceanic crust intrusives as a last step in a sequence of basaltic melt intrusion from pre-oceanic continental rifting to oceanic spreading.

Magmatic intrusions represented by Brothers and QUSEIR mafic complexes suggest the northern Red Sea is not a magma-poor rift, as generally believed. The sharp transition from continental crust to early sea floor spreading (Ligi et al., 2012), the lack of evidence for exhumed mantle, the short distance over which the crust thins from its reference thickness to the continent-ocean boundary (COB) with few fault blocks, point to a narrow rift with magmatic intrusions during rifting. A rifting model that captures many of the features observed in the central and northern Red Sea including the onset of seafloor spreading 24 Ma after the rift began, has been recently proposed (Allen and Beaumont, 2016). This numerical model with an extension rate of 10 mm/a includes the effects of evaporite syn-rift deposition preceded and followed by aggrading and prograding clastic sediment, and adopts an intermediate crust composition between strong and weak crust models (Huismans and Beaumont, 2011; Type I and Type II, i.e., narrow vs wide rifted margins) allowing some decoupling between the upper and lower crust.

Brothers and QUSEIR gabbros represent thinned-continental lower-crust intrusions of asthenospheric melt that will be later exposed at the seafloor during rifting. $^{40}Ar/^{39}Ar$ ages and isotopic composition of QUSEIR gabbros indicate that they may be related to the early syn rift intense magmatic event ~22 Ma, that gave rise to the dyke swarm running along the entire Arabian Red Sea coast (Bosworth et al., 2005; Bosworth and Stockli, 2016). This may have contributed to weaken the lower crust during early rifting favouring some decoupling between upper and lower crust, protracting upper crust extension and delaying crustal breakup. In a magmatic rift, extension is accommodated continuously in the ductile melt-rich lower crust by a combination of magmatic addition and viscous flow, favouring the rise at shallow levels of the asthenosphere (Wright et al., 2012). Numerical rifting models including frictional-plastic strain-softening for a moderately weak mid/lower crust with wet quartz rheology, predict an initial phase of distributed crustal extension as the crust decouples from the mantle with a weak early asymmetry, whereas during later stages the crust develops localized frictional shear zones forming fault blocks juxtaposed against mid/lower lithosphere in the upper crust and followed by symmetric lithosphere mantle necking and with no exposure of mantle lithosphere (Huismans and Beaumont, 2003). This scenario is in line with our observations and with the inferred crustal structure across the northern Red Sea based on P-wave

receiver functions and S-wave velocities showing a symmetric lithosphere mantle necking (Hosny and Nyblade, 2014). Recently, Liao and Gerya (2015) developed thermo-mechanical coupled visco-plastic numerical models to investigate extension from continental rifting to seafloor spreading, including inherited rheological structures of continental lithosphere (coupling/decoupling) and melt production during rifting. Models with decoupled initial rheology due to a weak lower crustal layer suggest rapid strain localization and dominant crustal thinning in the early rift stage. Lithospheric mantle extension becomes dominant after a short extension time leading to breakup of the lithosphere, indicating depth dependent extension (Huismans and Beaumont, 2011) and delaying crustal breakup. Fast lithospheric mantle thinning and wide asthenosphere upwelling induce decompression melting of the rising mantle leading to significant magmatic activity during rifting. The models generate numerous along strike heterogeneities during rifting caused by an inhomogeneous magma production. Regions with higher melt production rate rupture earlier in line with the hypothesis that continental rupture in the Red Sea occurs in a punctiform way (Bonatti et al., 1985). Melt production is highest in the very initial phases of oceanic crust accretion and becomes constant once seafloor spreading reaches a steady state, as observed at Thetis and Nereus in the central Red Sea (Ligi et al., 2011; 2012). Magma chambers below rift axis may also develop as we observed at Thetis.

The new results presented in this study provide rare constraints on the composition, depth of emplacement and age of early syn-rift magma intrusions into the deep crust, because they are available from near surface and borehole rocks; the northern Red Sea has experienced significant footwall uplift during rifting, which has ultimately brought early syn-rift deep crustal rocks to a suitable depth for sampling. Most constraints on the locus/depth of magma intrusion during the early stages of rifting derive from crustal scale seismic imaging of relatively young/poorly evolved rifts. For example the Baikal rift shows seismic evidence for solidified mafic intrusions into the lower crust with no upper crustal intrusions during the early rift phase (Thybo and Nielson, 2009). Another slightly more evolved example is the Ethiopian rift, where wide angle seismic refraction shows similarly high seismic velocities covering a large volume region of sub-rift lower crust, interpreted as significant lower crustal intrusion. However, the mid-upper crust shows a narrow

zone of elevated seismic velocities only beneath the current rift axis (Mackenzie et al., 2005). Observations from the Kenia rift where the axial volcanism is young (Quaternary to Recent, Thybo et al., 2000) suggest that the early stage of rifting is characterised by lower crustal intrusion, that becomes shallower and more focused axially through time (Mackenzie et al, 2005). However, while the overall evolutionary sequence is similar to that proposed here for the northern Red Sea, we have no direct age or compositional constraints on the intruded rocks. Instead, the approximate age of intrusions is inferred from the age and evolutionary stage of the rift, and the composition is interpreted from seismic velocities. In theory all the above examples of lower crustal intrusions could even be pre-rift, since no ages are available to prove that they are associated with rifting. A similar argument can be applied to most rifting passive margin where, for example, the age of lower crustal intrusions are approximated based on the position/depth of the intrusions in the post breakup crust, with the thinning crust at the rift axis assumed to be linked to progressive strain localisation into the axis. Crustal thickness, however, is measured from the final crustal thickness after breakup (White et al., 2008). This assumes a direct relationship between crustal thickness and rift evolution, which is probably correct to the first order of approximation, but again, is not direct evidence for age of intrusions.

5. Conclusions

We conclude that emplacement of oceanic melts in narrow rifts as the northern Red Sea, starts at depth during continental rifting, intruding the thinning continental crust before MORB erupts along the axial rift, initiating seafloor spreading. This model of pre-seafloor spreading MORB-type melt intrusions can be extended to the central Red Sea, where P-wave velocities of 6.6–6.9 km/s, similar to measured velocities of unaltered gabbros, have been observed from a deep refracting layer below Miocene evaporites, extending eastward outside the Thetis Deep to 65 km from the axis (Mitchell and Park, 2014; Tramontini and Davis, 1969). These concepts also can be applied to other narrow rifts: for instance, seismic reflection profiles across the eastern passive margin of north America detect consistently a ~7.2 km/s layer extending continuously beneath the thinning continental crust and merging seawards with oceanic layer 3, in agreement with a gabbroic unit

underplating the thinning continental crust before rupture in the North Atlantic rift (Kelemen and Holbrook, 1995).

Acknowledgements

Research sponsored by PRIN2012 Programme (Project 20125JKANY_002). Work supported by the Italian Consiglio Nazionale Ricerche and the US National Science Foundation. We are thankful to O. R. Berg for providing the gabbro sample from the QUSEIR B-1X drill hole. We thank R. Braga for major element analysis for the QUSEIR gabbro. We thank A. Argnani for helpful discussions, and J. Dyment and R. Huismans for constructive comments. We are particularly grateful to D. Keir, T. Gerya and Editor-in-Chief M. Santosh for helpful and constructive reviews that greatly improved the manuscript.

References

Allen, J., Beaumont, C., 2016. Continental margin syn-rift salt tectonics at intermediate width margins. Basin Research 28, 598–633, https://doi.org/10.1111/bre.12123.

Almalki, K.A., Betts, P.G., Ailleres, L., 2015. The Red Sea—50 years of geological and geophysical research. Earth Science Reviews 147, 109–140, https://doi.org/10.1016/j.earscirev. 2015. 05.002.

Almalki, K.A., Betts, P.G., Ailleres, L., 2016. Incipient seafloor spreading segments: Insights from the Red Sea. Geophysical Research Letters 43, 2709–2715, https://doi.org/10.1002/2016GL 068069

Andersen, D.J., Lindsley, D., Davidson, P.M., 1993. QUILF: a Pascal program to assess equilibria among Fe–Mg–Mn–Ti-oxides, pyroxenes, olivine, and quartz. Computers & Geosciences 19, 1333–1350, https://doi.org/10.1016/0098-3004(93)90033-2.

Aoki, K., Kushiro, I., 1968. Some clinopyroxenes from ultramafic inclusions in Dreiser Weiher, Eifel. Contributions to Mineralogy and Petrology 18, 326–337, https://doi.org/10.1007/BF 00399694.

Arevalo, R., McDonough, W.F., 2010. Chemical variations and regional diversity observed in MORB. Chemical Geology 271, 70–85.

Bonatti, E., 1985. Punctiform initiation of seafloor spreading in the Red Sea during transition from continental to an oceanic rift. Nature 316, 33–37, https://doi.org/10.1038/316033a0.

Bonatti, E., Colantoni, P., Della Vedova, B., Taviani, M., 1984. Geology of the Red Sea transitional region (22°-25°N). Oceanologica Acta 7, 385–398.

Bonatti, E., Seyler, M., 1987. Crustal underplating and evolution in the Red Sea rift. Journal of Geophysical Research 92, 12083–12821, https://doi.org/10.1029/JB092iB12p12803.

Bonatti, E., Ottonello, G., Hamlyn, P.R., 1986. Peridotites from the island of Zabargad (Red Sea). Journal of Geophysical Research 91, 599–631, https://doi.org/10.1029/JB091iB01p00599.

Bosworth, W., 1993. Nature of the Red Sea crust. A controversy revisited: comment and reply. Geology 21, 574–575, https://doi.org/10.1130/0091-7613(1993)021<0574:NOTRSC>2.3.CO;2.

Bosworth, W., Darwish, M., Crevello., P., Taviani, M., Marshak, S., 1996. Stratigraphic and structural evolution of Zabargad Island (Red Sea, Egypt) since the Early Cretaceous. In: El.

Youssef, S. A. (Ed), *Proceedings of the Third International Conference on Geology of the Arab World*. Cairo University Vol. 1, pp 161–190.

Bosworth, W., Huchon, P., McClay, K., 2005. The Red Sea and Gulf of Aden basins. Journal of African Earth Sciences 43, 334–378, https://doi.org/10.1016/j.jafrearsci.2005.07.020.

Bosworth, W., Stockli, D.F., 2016. Early magmatism in the greater Red Sea rift: timing and significance. Canadian Journal of Earth Sciences 53, 1158–1176, https://doi.org/10.1139/cjes-2016-0019.

Chu, D., Gordon, R.G., 1998. Current plate motions across the Red Sea. Geophysical Journal International 135, 313-328, https://doi.org/10.1046/j.1365-246X.1998.00658.x.

Cochran, J.R., 1983. A model for the development of the Red Sea. AAPG Bulletin 67, 41–69.

Cochran, J.R., 2005. Northern Red Sea: Nucleation of an oceanic spreading center within a continental rift. Geochemistry Geophysics Geosystems 6, Q03006, http://dx.doi.org/10.1029/2004GC000826.

Cochran, J.R., Martinez, F., 1988. Evidence from the northern Red Sea on the transition from continental to oceanic rifting. Tectonophysics 153, 25–53, https://doi.org/10.1016/0040-1951(88)90006-6.

Crane, K., Bonatti, E., 1987. The role of fracture zones during early Red Sea rifting: Structural analysis using Space Shuttle radar and LANDSAT imagery. Journal of the Geological Society 144, 407–420, https://doi.org/10.1144/gsjgs.144.3.0407.

Dalrymple, G.B., Alexander, E.C., Lanphere, M.A., Kraker, G.P., 1981. Irradiation of samples for $^{40}Ar/^{39}Ar$ dating using the geological survey TRIGA reactor. USGS Professional Papers, Vol. 1176, U.S. Geological Survey, Reston, VA, United States, pp. 29.

Deniel, C., Vidal, P., Coulon, C., Vellutini, P.J., Piguet, P., 1994. Temporal evolution of mantle sources during continental rifting: the volcanism of Djibouti (Afar). Journal of Geophysical Research 99, 2853-2869, https://doi.org/10.1029/93JB02576.

Detrick, R.S., Buhl, P., Vera, E., Mutter, J., Orcutt, J., Madsen, J., Brocher, T., 1987. Multi-channel seismic imaging of a crustal magma chamber along the East Pacific Rise. Nature 326, 35–41, https://doi.org/10.1038/326035a0.

Dyment, J., Tapponnier, P., Afifi, A. M., Zinger, M. A., Franken, D., Muzaiyen, E., 2013. A New Seafloor Spreading Model of the Red Sea: Magnetic Anomalies and Plate Kinematics. AGU Fall Meeting 2013, San Francisco, T21A-2512.

Ehrhardt, A., Hubscher, C., 2015. The Northern Red Sea in Transition from Rifting to Drifting-Lessons Learned from Ocean Deeps. In: Rasul, N.M.A., Stewart, I.C.F. (Eds.), *The Red Sea: The Formation, Morphology, Oceanography and Environ-ment of a Young Ocean Basin*. Springer-Verlag, Berlin, Heidelberg, pp. 135–121, https://doi.org/10.1007%2F978-3-662-45201-1_5.

El-Bohoty, M., Brimich, L., Saleh, A., Saleh, S., 2012. Comparative study between the structural and tectonic situation of the Southern Sinai and the Red Sea, Egypt, as deduced from magnetic, gravity and seismic data. Contributions to Geophysics and Geodesy 42, 357-388.

Ernst, W.G., Liu, J., 1998. Experimental phase-equilibrium study of Al- and Ti-contents of calcic amphibole in MORB-A semiquantitative thermobarometer. American Mineralogist 83, 952–969.

Féménias, O., Mercier, J.C.C., Nkono, C., Diot, H., Berza, T., Tatu, M., Demaiffe, D., 2006. Calcic amphibole growth and compositions in calc-alkaline magmas: evidence from the Motru Dike Swarm (Southern Carpathians, Romania). American Mineralogist 91, 73–81.

Frost, B.R., Lindsley, D.H., 1992. Equilibria among Fe–Ti oxides, pyroxenes, olivine, and quartz: part II. Application. American Mineralogist 77, 1004–1020.

Gaulier, J. M., LePichon, X., Lyberis, N., Avedik, F., Geli, L., Moretti, I., Deschamps, A., Hafez S., 1988. Seismic study of the crustal thickness, Northern Red Sea and Gulf of Suez. Tectonophysics 153, 55–88.

Ghebreab, W., 1998. Tectonics of the Red Sea region reassessed. Earth Science Reviews 45, 1–44, https://doi.org/10.1016/S0012-8252(98)00036-1.

Girdler, R.W., 1985. Problems concerning the evolution of oceanic lithosphere in the northern Red Sea. Tectonophysics 116, 109–122, https://doi.org/10.1016/0040-1951(85)90224-0.

Girdler, R.W., Styles, P., 1974. Two stage seafloor spreading. Nature 247, 7–11, https://doi.org/10.1038/247007a0.

Gordon, G., Hansen, B., Scott, J., Hirst, C., Graham, R., Grow, T., Spedding, A., Fairhead, S., Fullarton, L., Griffin, D., 2010. The hydrocarbon prospectivity of the Egyptian North Red Sea

basin. In: Vining, B.A., Pickering, S.C. (Eds), *Petroleum Geology: From Mature Basins to New Frontiers*, Proceedings of the 7th Petroleum Geology Conference, Geological Society of London, pp. 783–789.

Guennoc, P., Pautot, G., Coutelle, A., 1988. Surficial structures of the northern Red Sea axial valley from 23°N to 28°N: Time and space evolution of neo-oceanic structures. Tectonophysics 153, 1–23, https://doi.org/10.1016/0040-1951(88)90005-4.

Kelemen, P., Holbrook, W., 1995. Origin of thick, high-velocity igneous crust along the U.S. East Coast margin. Journal of Geophysical Research 100, 10077–10094, https://doi.org/10.1029/95JB00924.

Haase, K.M., Muhe, R., Stoffers, P., 2000. Magmatism during extension of the lithosphere: geochemical constraints from lavas of the Shaban Deep, northern Red Sea. Chemical Geology 166, 225–239, https://doi.org/10.1016/S0009-2541(99)00221-1.

Hebert, R., Constantin, M., Robinson, P.T., 1991. Primary mineralogy of Leg 118 gabbroic rocks and their place in the spectrum of oceanic mafic igneous rocks. In: Von Herzen, R.P., Robinson P.T. et al. (Eds), *Proceedings of Ocean Drilling Program, Scientific Results,* Ocean Drilling Program, College Station TX, Vol. 118, pp. 3–20.

Hoang, C.T., Taviani, M., 1991. Stratigraphic and tectonic implications of uranium-series dated coral reefs from uplifted Red Sea islands. Quaternary Research 35, 264–273, https://doi.org/10.1016/0033-5894(91)90072-D.

Hosny, A., Khaled, O., Sherif, M.A., 2013. The Gulf of Suez earthquake, 30 January 2012, northeast of Egypt. Rendiconti Lincei 24, 377–386, https://doi.org/10.1007/s12210-013-0244-2.

Hosny, A., Nyblade, A., 2014. Crustal structure in southeastern Egypt: Symmetric thinning of the northern Red Sea rifted margins. Geology 42, 219–222, https://doi.org/10.1130/G34726.1.

Huismans, R.S., Beaumont, C., 2003. Symmetric and asymmetric lithospheric extension: Relative effects of frictional-plastic and viscous strain softening. Journal of Geophysical Research 108, 2496, https://doi.org/10.1029/2002JB002026.

Huismans, R.S., Beaumont, C., 2011. Depth-dependent extension, two-stage breakup and cratonic underplating at rifted margins. Nature 473, 74–78, https://doi.org/10.1038/nature09988.

LaBrecque, J.L., Zitellini, N., 1985. Continuous sea-floor spreading in Red Sea: An alternative interpretation of magnetic anomaly patterns. AAPG Bulletin 69, 513–524.

Liao, J., Gerya, T., 2015. From continental rifting to seafloor spreading: insight from 3D thermo-mechanical modeling. Gondwana Research 28, 1329–1343.

Ligi, M., Bonatti, E., Bortoluzzi, G., Cipriani, A., Cocchi, L., Caratori Tontini, F., Carminati, E., Ottolini, L., Schettino, A., 2012. Birth of an ocean in the Red Sea: Initial pangs. Geochemistry Geophysics Geosystems 13, Q08009, https://doi.org/10.1029/2012GC004155.

Ligi, M., Bonatti, E., Caratori Tontini, F., Cipriani, A., Cocchi, L., Schettino, A., Bortoluzzi, G., Ferrante, V., Khalil, S. M., Mitchell, N.C., Rasul, N., 2011. Initial burst of oceanic crust accretion in the Red Sea due to edge-driven mantle convection. Geology 39, 1019–1022, https://doi.org/10.1130/G32243.1.

Ligi, M., Bonatti, E., Rasul N.M.A., 2015. Seafloor Spreading Initiation: Geophysical and Geochemical Constraints from the Thetis and Nereus Deeps, Central Red Sea. In: Rasul, N.M.A., Stewart, I.C.F. (Eds), *The Red Sea: The Formation, Morphology, Oceanography and Environ-ment of a Young Ocean Basin*. Springer-Verlag, Berlin, Heidelberg, pp. 79–98, https://doi.org/10.1007%2F978-3-662-45201-1_4.

Ligi, M., Bortoluzzi, G., 1989. PLOTMAP: Geophysical and geological applications of good standard quality cartographic software. Computers & Geosciences 15, 519–585, https://doi.org/10.1016/0098-3004(89)90023-X.

Lindsley, D.H., 1983. Pyroxene thermometry. American Mineralogist 68, 477–493.

Loucks, R.R., 1996. A precise olivine-augite Mg-Fe-exchange geothermometer. Contributions to Mineralogy and Petrology 125, 140–150.

Mackenzie, G.D., Thybo, H., Maguire, P.K.H., 2005. Crustal velocity structure across the Main Ethiopian Rift: results from two-dimensional wide-angle seismic modelling. Geophysical Journal International 162, 994–1006, https://doi.org/10.1111/j.1365-246X.2005.02710.x.

McGuire, A.V., Coleman, R.G., 1986. The Jabal Tirf layered gabbro and associated rocks of the Tihama Asir complex. SW Saudi Arabia. Journal of Geology 94, 651–665.

Mitchell, N.C., Ligi, M., Feldens, P., Hubscher, C., 2017. Deformation of a young salt giant: regional topography of the Red Sea Miocene evaporites. Basin Research 29, 352–369, https://doi.org/10.1111/bre.12153.

Mitchell, N.C., Ligi, M., Ferrante, V., Bonatti, E., Rutter, E., 2010. Submarine salt flows in the central Red Sea. Geological Society of America Bulletin 122, 701–713, https://doi.org/10.1130/B26518.1.

Mitchell, N.C., Park, Y., 2014. Nature of crust in central Red Sea. Tectonophysics 628, 123-139, https://doi.org/10.1016/j.tecto.2014.04.029.

Mooney, W.D., Gettings, M.E., Blank, H.R., Healy, J.H., 1985. Saudi Arabian seismic refraction profile: a traveltime interpretation of crustal and upper mantle structure. Tectonophysics 111, 173-246, https://doi.org/10.1016/0040-1951(85)90287-2.

Nicolas, A., Boudier, F., Lyberis, N., Montigny, R., and Guennoc, P., 1985. L'île de Zabargad (Saint-Jean): témoin clé de l'expansion précoce en Mer Rouge. Comptes Rendus de l'Academie des Sciences, Serie 2, 301, 1063–1068.

Nimis, P., 1999. Clinopyroxene geobarometry of magmatic rocks: Part 2. Structural geobarometers for basic to acid, tholeiitic and mildly alkaline magmatic systems. Contributions to Mineralogy and Petrology 135, 62–74, https://doi.org/10.1007/s004100050498.

Nimis, P., Ulmer, P., 1998. Clinopyroxene geobarometry of magmatic rocks, Part 1: An expanded structural geobarometer for anhydrous and hydrous, basic and ultrabasic systems. Contributions to Mineralogy and Petrology 133, 314–327, https://doi.org /10.1007/s004100050442.

Parker, R.L., 1973. The rapid calculation of potential anomalies. Geophys. J. R. Astr. Soc. 31, 447–455.

Petrini, R., Joron, J.L., Ottonello G., Bonatti E., Seyler M., 1988. Basaltic dykes from Zabargad Island, Red Sea: petrology and geochemistry. Tectonophysics 150, 229–248, https://doi.org/ 10.1016/0040-1951(88)90303-4.

Prada, M., Sallares, V., Ranero, C.R., Vendrell, M.G., Grevemeyer, I., Zitellini, N., de Franco, R., 2015. The complex 3-D transition from continental crust to backarc magmatism and exhumed mantle in the Central Tyrrhenian basin. Geophysical Journal International 203, 63–78, https://doi.org/10.1093/gji/ggv271.

Purdy, G.M:, Kong, L.S.L., Christeson, G.L., Solomon, S.C., 1992. Relationship between spreading rate and the seismic structure of mid-ocean ridges. Nature 355, 815-817, https://doi.org/ 10.1038/355815a0.

Renner, L.C., Hartmann, L.A., Wildner, W., Massonne, H.-J., Theye, T., 2011. A micro-analytical approach to partition coefficients in plagioclase and clinopyroxene of basaltic sills in Serra Geral Formation, Paraná Basin, Brazil. Revista Brasileira de Geociências 41, 263–289.

Sallares,V., Martínez-Loriente, S., Prada, M., Gràcia, E., Ranero, C., Gutscher, M.-A., Bartolome, R., Gailler, A., Dañobeitia, J.J., Zitellini, N., 2013. Seismic evidence of exhumed mantle rock basement at the Gorringe Bank and the adjacent Horseshoe and Tagus abyssal plains (SW Iberia). Earth Planetary Science Letters 365**,** 120–131, https://doi.org/10.1016/j.epsl. 2013.01.021.

Sandwell, D.T., Muller, R.D., Smith, W.H.F., Garcia, E., Francis, R., 2014. New global marine gravity model from CryoSat-2 and Jason-1 reveals buried tectonic structure. Science 346, 65–67, https://doi.org/10.1126/science.1258213.

Seyler, M., Bonatti, E., 1988. Petrology of the gneissamphibolite metamorphic unit from Zabargad island, Red Sea. Tectonophysics 150, 177–207, https://doi.org/10.1016/0040-1951(88)90301-0.

Shukri, N.M., 1944. On the geology of the Brothers Islets-Northern Red Sea. Bull. Fac. Sci. Cairo Univ. 25, 175-196.

Singh, S.C., Crawford, W.C., Carton, H., Seher, T., Combier, V., Cannat, M., Canales, J.P., Dusunur, D., Escartin, J., Miranda, M., 2006. Discovery of a magma chambre and faults beneath a Mid-Atlantic Ridge hydrothermal field. Nature 442, 1029-1032, https://doi.org/ 10.1038/nature05105.

Sultan, M., Becker, R., Arvidson, R.E., Sore, P., Stern, R.J., El-Alfy, Z., Guinnes, E.A., 1992. Nature of the Red Sea crust, a controversy revisited. Geology 20, 593–596, https://doi.org/ 10.1130/0091-7613(1992)020<0593:NOTRSC>2.3.CO;2.

Tapponnier, P., Dyment, J., Zinger, M.A., Franken, D., Afifi, A.M., Wyllie, A., Ali, H.G., Hanbal, I., 2013. Revisiting seafloor-spreading in the Red Sea: basement nature, transforms and ocean-continent boundary. AGU Fall Meeting 2013, San Francisco, T12B-04.

Thybo, H., Nielsen, C.A., 2009. Magma-compensated crustal thinning in continental rift zones. Nature 457, 873–876, https://doi.org/10.1038/nature07688.

Thybo, H., Maguire, P.K.H., Birt, C., Perchuc, E., 2000. Seismic reflectivity and magmatic underplating beneath the Kenya Rift. Geophysical Research Letters 17, 2745–2748, https://doi.org/10.1029/1999GL011294.

Todt, W., Cliff, R.A., Hanser, A., Hofmann, A.W.. 1996. Evaluation of a ^{202}Pb-^{205}Pb double spike for high precision lead isotopic analysis. In Basu, A., Hart, S. (Eds), *Earth Processes: Reading the Isotopic Code*. AGU Geophysical Monograph 95, American Geophysical Union, Washington DC, 429–437.

Tramontini, C., Davis, D., 1969. A seismic refraction survey in the Red Sea. Geophys. J. R. Astr. Soc. 17, 225-241.

Villa, I.M., 1990. ^{40}Ar/^{39}Ar dating of amphiboles from Zabargad Island (Red Sea) is precluded by interaction with fluids. Tectonophysics 180, 369–373, https://doi.org/10.1016/0040-1951(90)90319-4.

Volker, F., McCulloch, M.T., 1993. Submarine basalts from the Red Sea: New Pb, Sr, and Nd isotopic data. Geophysical Research Letters 20, 927–930, https://doi.org/10.1029/93GL00050.

Wegener, A., 1929. Die Entstehung der Kontinente und Ozeane, *4th edition*, Braunschweig: Friedrich Vieweg & Sohn.

White, R.S., McKenzie, D., O'Nions, R.K., 1992. Oceanic crustal thickness from seismic measurements and rare earth element inversions. Journal of Geophysical Research 97**,** 19683–19715, https://doi.org/10.1029/92JB01749.

White, R.S., Smith, L., Roberts, A., Christie, P., Kusznir, N., and iSIMM, Team, 2008. Lower–crustal intrusion on the North Atlantic continental margin. Nature 452, 460–464, https://doi.org/10.1038/nature06687.

Wright, T., Sigmundsson, F., Ayele, A., Belachew, M., Brandsdottir, B., Calais, E., Ebinger, C., Einarsson, P., Hamling, I., Keir, D., Lewi, E., Pagli, C., Pedersen, R., 2012. Geophysical constraints on the dynamics of spreading centres from rifting episodes on land. Nature Geoscience 5, 242–250, https://doi.org/10.1038/ngeo1428.

Figure Captions

Figure 1. Topography of the northern Red Sea and its main morphotectonic features. Plate separation rates of Arabia from Nubia range from 12.1 mm/yr at Thetis to 9 mm/yr at Brothers (Chu and Gordon, 1998). White dots, earthquake epicentres with magnitude > 3 since 1976, from International Seismological Data Centre. The numbered black box refers to the area displayed in figures 2a and 2b. The labelled red polygon marks location of the 3D seismic survey. The red circle indicates the location of the Phillips oil well QUSEIR B-1X and the numbered black line marks the location of seismic cross-line 3170 shown in figure 2c. Thick red dashed lines: Zabargad Shear Zone. Location of seismic reflection profile TL-23M (figure 4) is indicated. Top right inset: simplified plate tectonic framework of the Red Sea/Gulf of Aden area: dark areas, oceanic crust.

Figure 2. Morphotectonic setting of Brothers Islets region. Bathymetry, morphology and seismic images show the transtensional origin of the Oceanographer Deep and the ongoing tectonics causing uplift of the crustal blocks culminating in the two Brothers islets and in the structural high located to southwest of the islets. The Oceanographer Deep is located east of the two crustal blocks at the intersection of a left stepping transcurrent fault with Dead Sea Transform direction and a NE dextral transcurrent fault oriented normal to the present day rift axis. The recent uplift of the two crustal blocks is due to extension associated to splay faults at the southern end of the NE dextral transcurrent fault. (**a-b**) shaded relief image from a compilation of single beam and multibeam bathymetry together with water depth obtained by converting to depth the two way travel time of the 3D seismic seafloor reflector using a constant water velocity of 1.525 km/s. Source of light from NE, grid resolution 25 m. (**c-d**) Time migrated seismic cross-line 3170 extracted from the 3D seismic survey and running perpendicular to the axis of the Northern Red Sea and to the crustal block lying to the southwest of

Brothers Islets. Full profile location is indicated in Figure 1. **c**, Processed data only; d, interpretation of the processed data. The Brothers islets reached present level before 125 ka and since then they have been tectonically quiescent (Hoang and Taviani, 1991). However, a Plio-Quaternary uplift of the southwestern crustal block is shown in seismic crossline #3170. In fact, the Miocene evaporites are absent on the NE flank of the tilted block and the Plio-Quaternary sequence is following conformably the tilting of the basement.

Figure 3. Geochemistry of Brothers and QUSEIR gabbros. Major, trace elements and isotopic geochemical data suggest a MORB-like composition with no contamination by continental lithospheric components. (**a**) Sr-Nd isotopic composition superimposed on global MORB data (gray field), on basalt data from the Red Sea axis (purple field), from the Red Sea southern islands (blue field) and from the Afar (yellow field). (**b**) C1 chondrite–normalized REE patterns for cpx. Calculated cpx in equilibrium with N-MORB (Arevalo and McDonough, 2010) are shown by a black dotted line; cpx/liquid partition coefficients used in the calculation are from Renner et al. (2011). (**c**) A (Na_2O+K_2O) - M (MgO) - F (FeO_{tot}) plot: Brothers gabbros (red diamond) and dolerites (gray triangle), QUSEIR gabbros (green circle), Zabargad pyroxenites and gabbros (Seyler and Bonatti, 1988; Petrini et al., 1988) (yellow square) and gabbroic rocks from Jabal Tirf (McGuire and Coleman, 1986) (open blu cross). Yellow and gray filled areas indicate compositions of gabbroic rocks from ODP hole 1109A and of gabbroic cumulates from ophiolites and from Mid-Atlantic and Southwest Indian ridges, respectively.

Figure 4. A magma chamber below the axis of Thetis Deep. Multichannel seismic line TL-23M perpendicular to the axis of the southern Thetis basin showing a prominent reflector about 1.3–1.5 s below the axial neo-volcanic zone interpreted as marking the roof of a magma chamber. Assuming a 4.5 km/s

acoustic velocity for the upper oceanic crust at Thetis (Tramontini and Davis, 1969), this reflector is ~3.2 km below the seafloor, implying that the top of the inferred magma chamber lies deeper than those identified below fast spreading ridges such as the East Pacific Rise (Detrick et al., 1987). Profile location is indicated as a numbered black solid line in Figure 1. (**a**) finite-difference time migrated section. Left inset: detail focusing on the interpreted magma chamber. Right inset: stack section. The reflector from the top of the axial magma chamber (AMC) has polarity opposite to that of the seafloor reflector because of the seismic velocity reduction due to presence of melt below. Wiggle traces show the polarity of the different reflections. (**b**) interpreted line drawing. The extension of the oceanic crust beneath evaporites is inferred from magnetic data.

Figure 5. Gravity anomalies of the Northern Red Sea. **(a)** free air anomalies from satellite-derived gravity data (Sandwell et al., 2014; version 23.1). **(b)** Bouguer anomalies from free air data corrected for seabed topography using a density contrast of 1630 kg/m^3 . The contribution of topography to the local gravity field has been computed from grids of bathymetry by a FFT technique, that uses a series expansion of the Fourier transformed powers of the base of each layer to represent the Fourier transform of the gravity anomaly (Parker, 1973). The first nine terms of the series expansion were retained in our calculations to account for the non-linear gravitational attraction of the large topographic relief.

Figure 6. QUSEIR gabbros $^{40}Ar/^{39}Ar$ age determination. (**a-b**) Representative age spectra and isochron plots derived from $^{40}Ar/^{39}Ar$ incremental heating experiments on the QUSEIR gabbros. The plateau age (±1σ) is calculated from the weighted mean of individual step ages whose width represents the fraction of the ^{39}Ar released. The vertical error bars represent 95% confidence interval. The isochron age that includes all the heating steps is slightly younger age, albeit within error of the plateau age and with an initial $^{40}Ar/^{36}Ar$ similar to air.

Figure 7. Seismicity and seismic crustal velocities of the northern Red Sea. (**a**) Epicenters recorded during 1973-2017 from International Seismological Centre, *On-line Bulletin* (http://www.isc.ac.uk, Internatl. Seismol. Cent., Thatcham, United Kingdom, 2014). Black filled diamonds show offshore wells where african basement rocks have been encountered at total depth: white numbers from Bosworth (1993) and yellow numbers from Almalki et al. (2015). Brothers and QUSEIR (white diamond) MORB-gabbros location is also indicated. White filled circles and black lines indicate Common Mid Points (CMP) and profile locations of two ships expanded spread profiles of Gaulier et al. (1988). (**b)** ESP vertical velocity profiles (Gaulier et al., 1988) compared with P-wave velocity-depth envelopes from different domains. Velocity structures for Arabia 35 km-thick continental crust (Mooney et al., 1985), for young oceanic crust (White et al., 1992), for thinned continental crust (Prada et al., 2015) and for exhumed mantle (Prada et al., 2015; Sallares et al., 2013) are indicated as colored curves marking the lateral variability of velocity within the given region.

Figure 8. Evolution of continental lower crust during rifting. Cartoon showing progressive shallower intrusions and/or underplating of the thinned continental crust by gabbroic, MORB-type melts before continental rupture and initial accretion of oceanic crust. Yellow, continental crust; gray, lithospheric mantle; red, magmatic intrusions; and green, gabbros and dykes.

Table 1. Major and trace elements for Brothers and QUSEIR gabbros.

Table 2. Nd, Sr, Pb, Sm isotopic data for Brothers and QUSEIR gabbros.

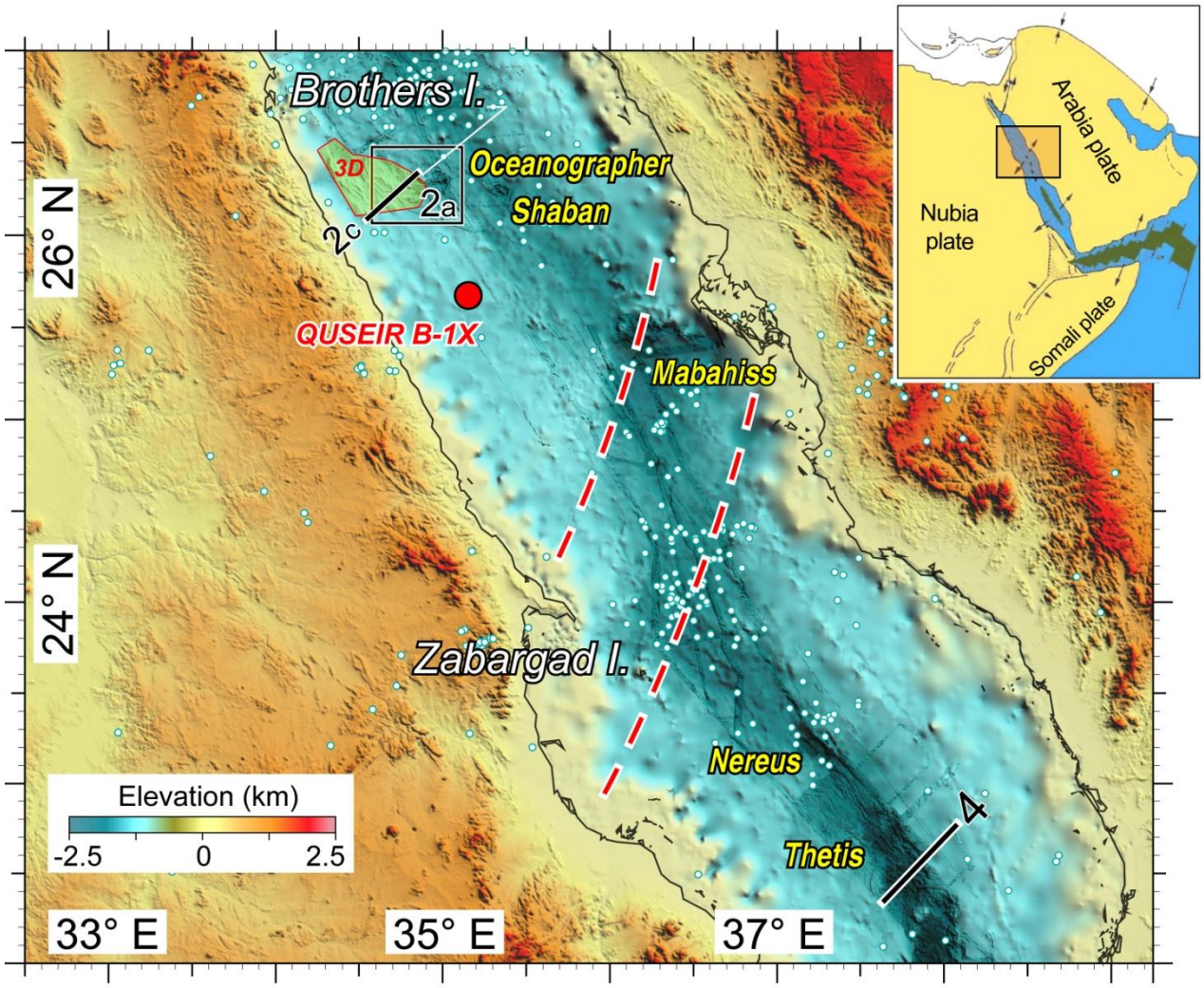

Figure 1

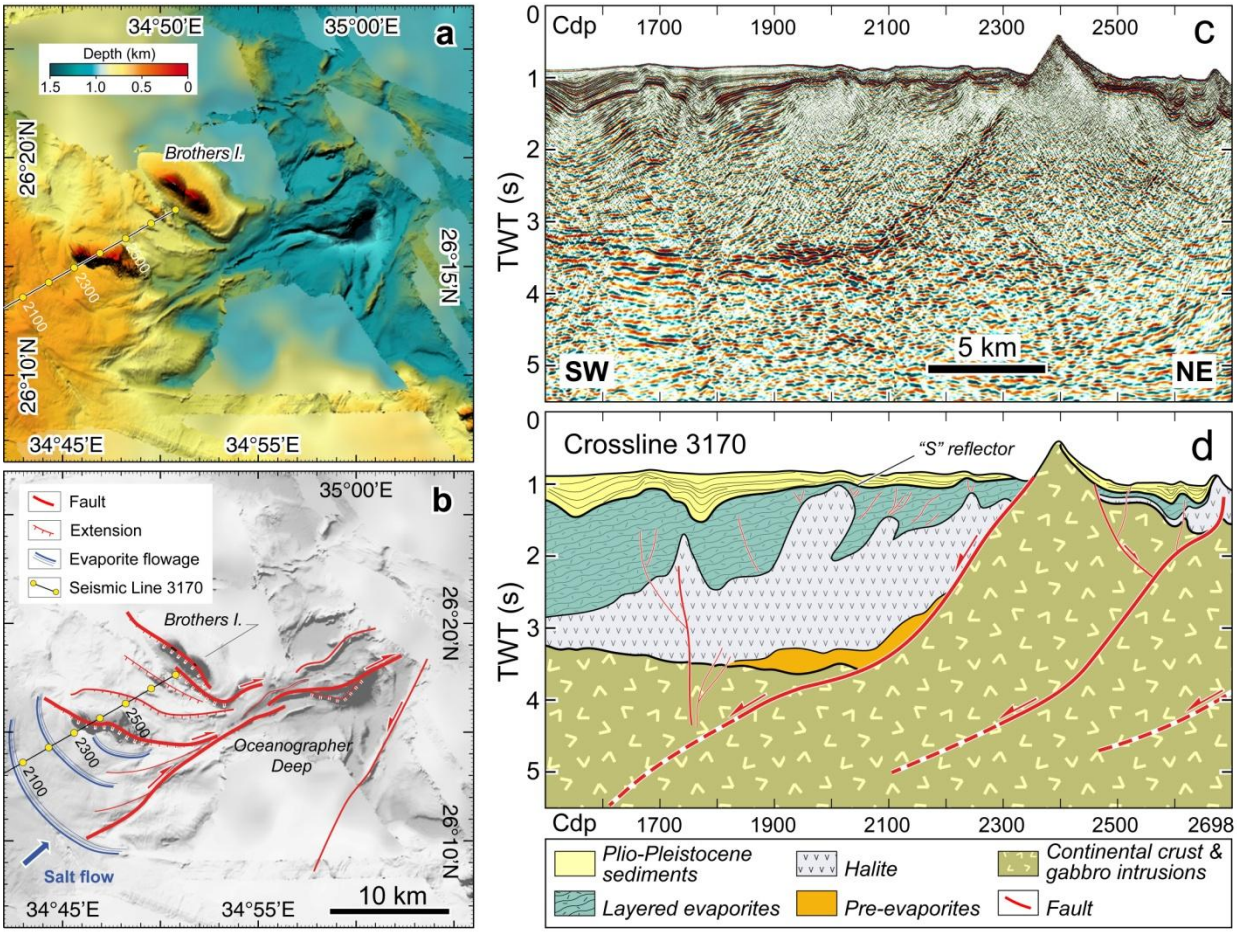

Figure 2

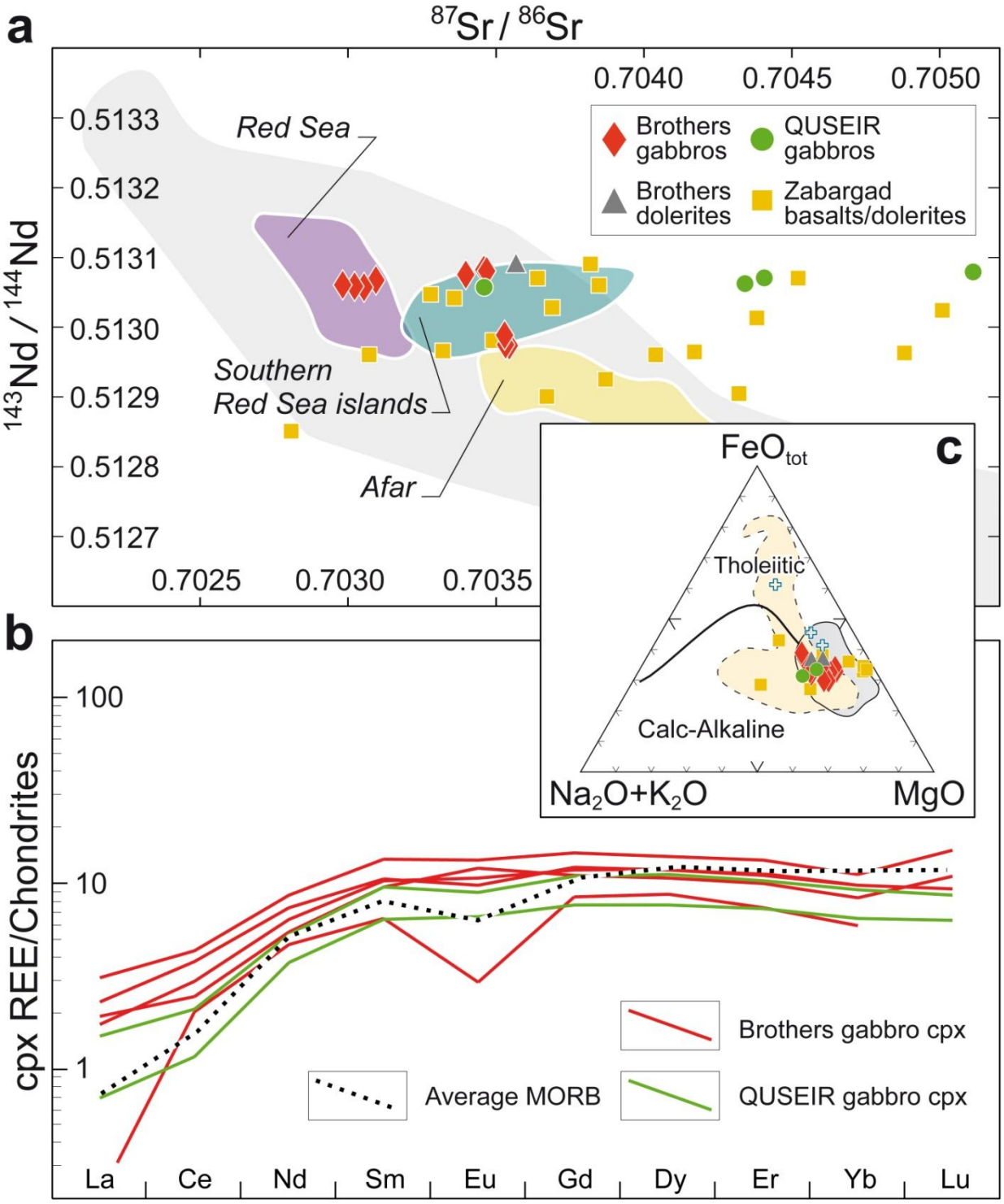

Figure 3

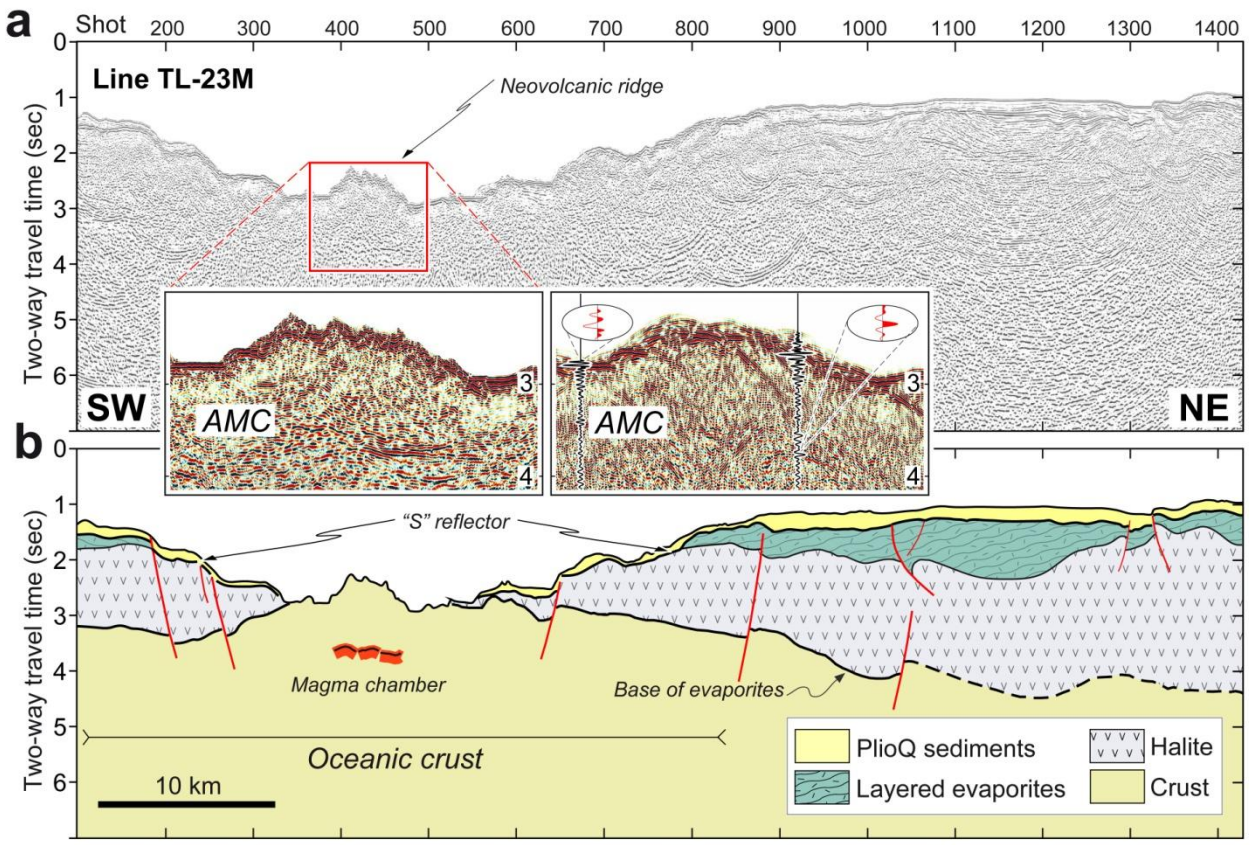

Figure 4

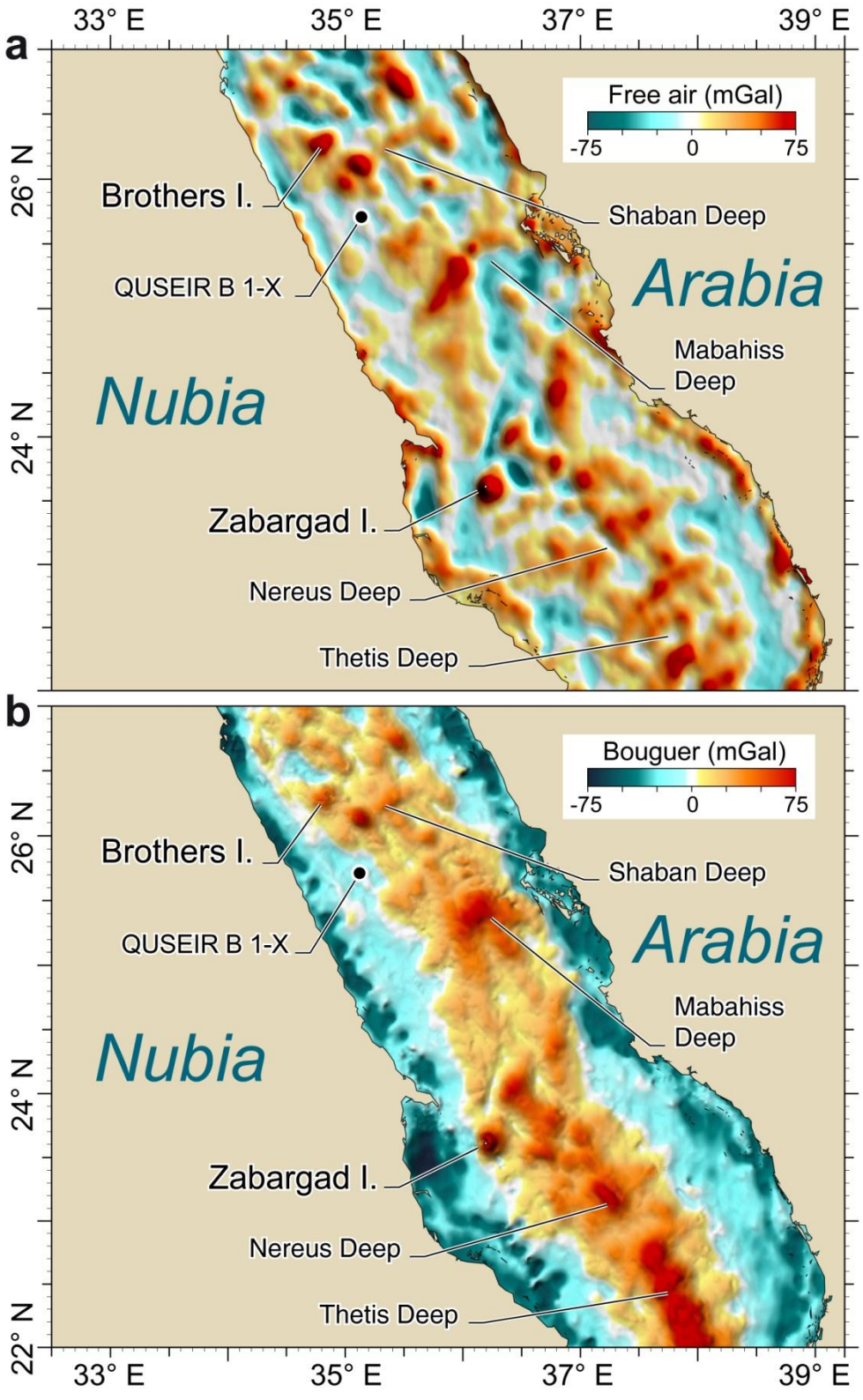

Figure 5

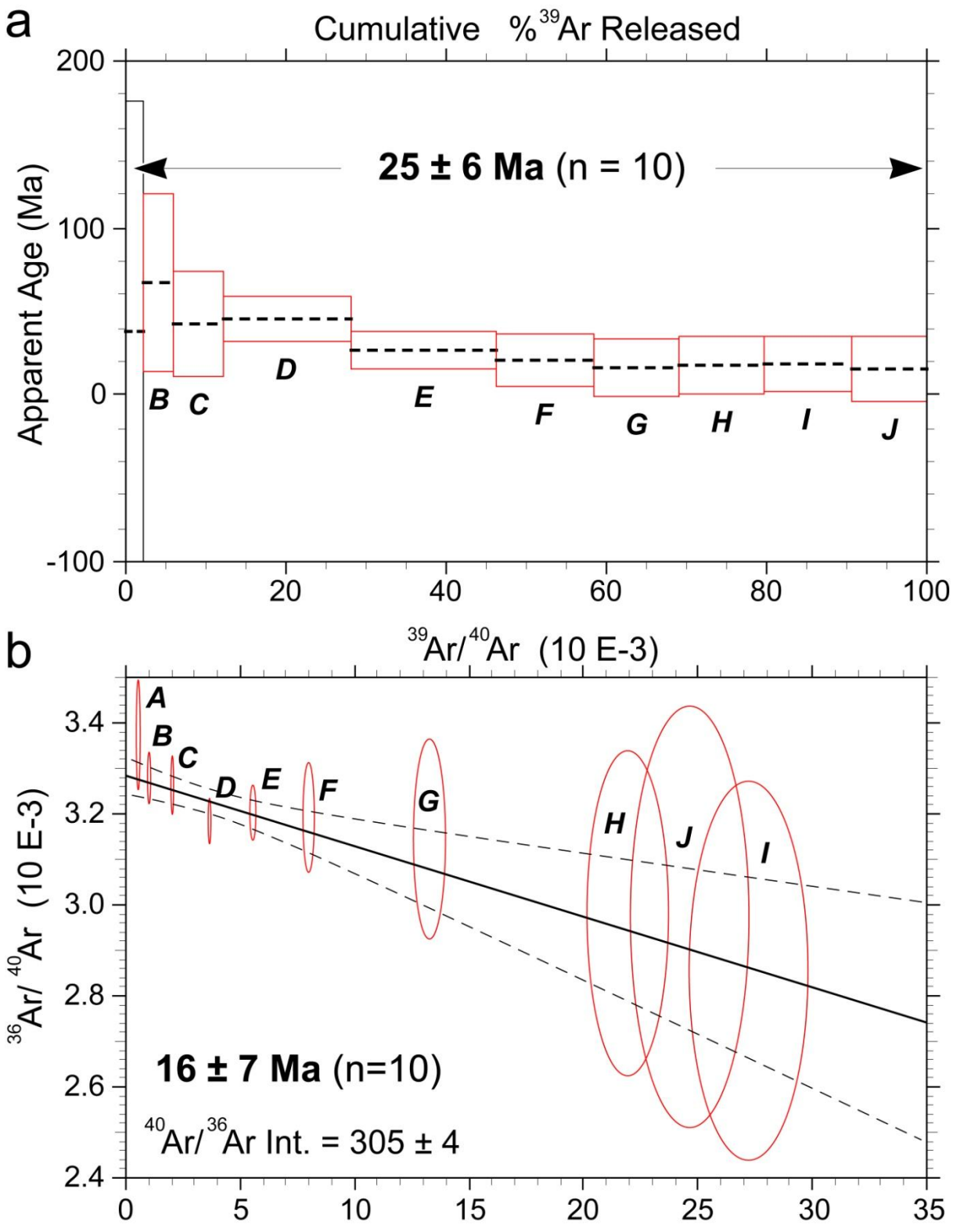

Figure 6

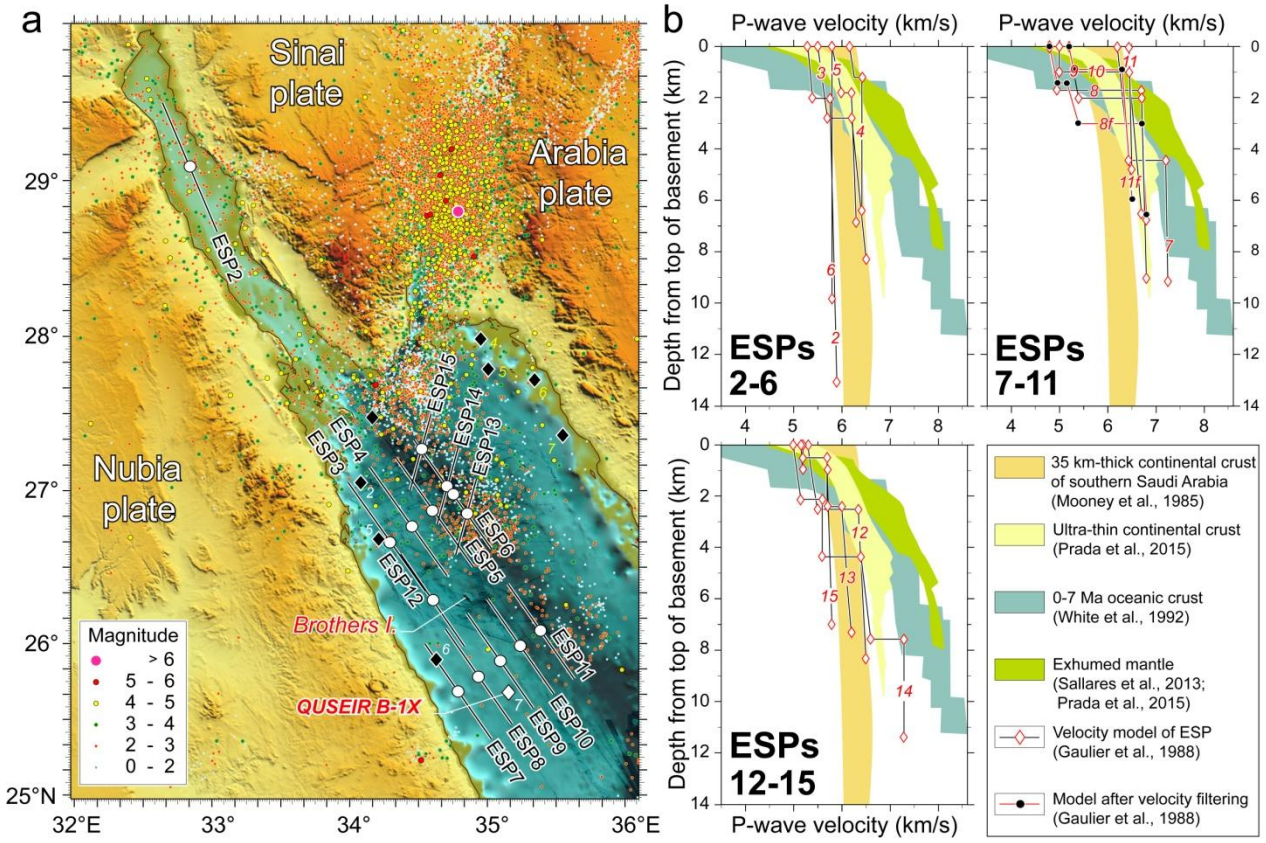

Figure 7

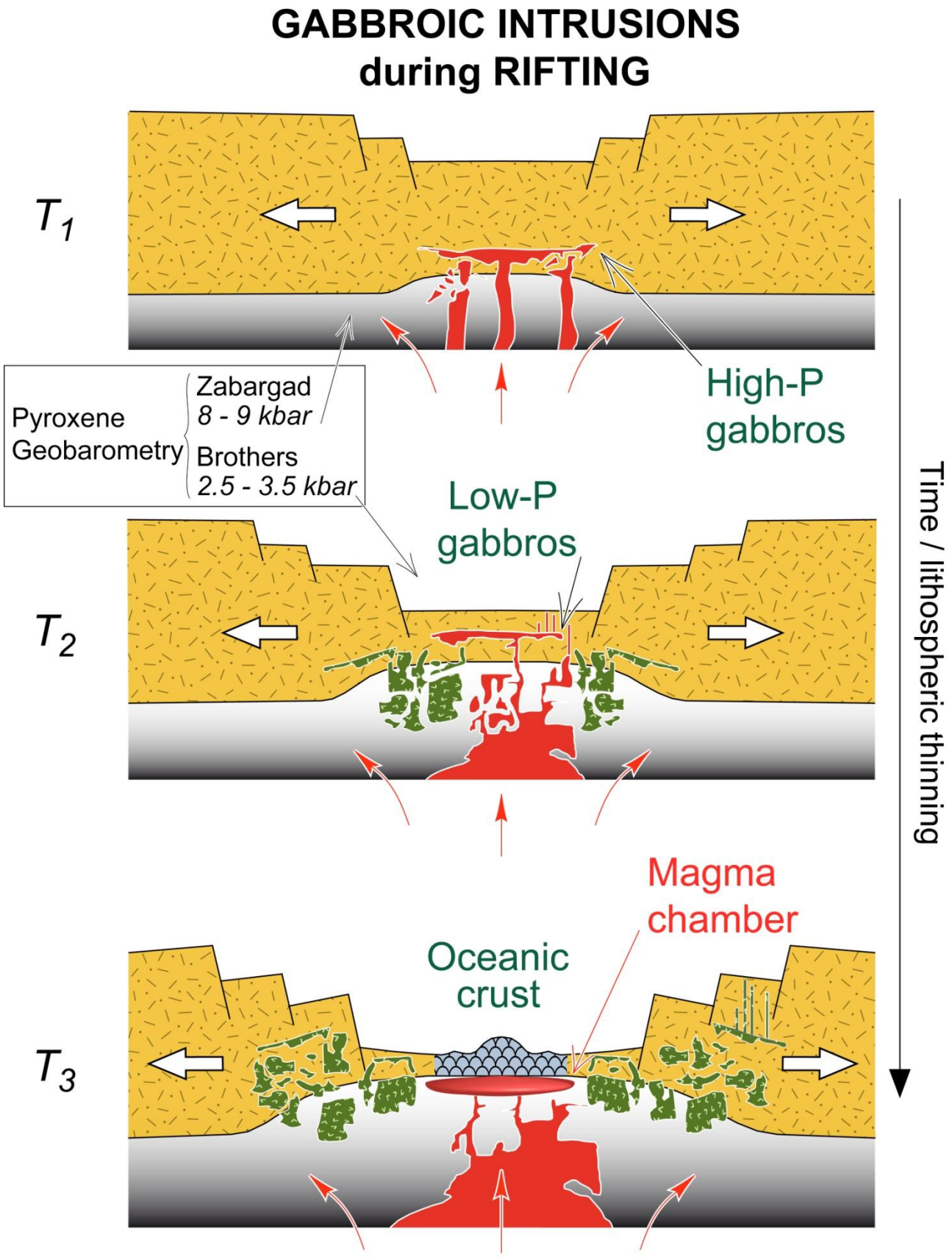

Figure 8

Table 1

	Brothers gabbros									Quseir gabbro
Rock type	m/cgr-G	mgr-G	mgr-OlG	m/cgr-OlG	cgr-G	cgr-G	cgr-G	cgr-OlLG	D	m/cgr OlLG
Sample	**BRO14-5-7**	**BRO14-5-8**	**BRO14-5-7A**	**BRO14-5-7B**	**BRO-A**	**BRO-BII**	**BRO-B**	**BRO-28**	**B-8**	**QUSEIR-B (I-X)**
SiO_2	49.74	49.77	49.59	49.82	50.51	50.16	49.75	49.75	47.71	47.02
TiO_2	0.241	0.284	0.247	0.280	0.46	0.40	0.36	0.72	0.89	0.55
Al_2O	16.60	18.22	16.28	15.79	16.75	21.34	21.23	19.58	16.74	23.25
Fe_2	1.21	0.42	0.96	0.57	--	--	--	--	--	--
FeO	5.34	5.41	5.75	6.32	--	--	--	--	--	--
FeOt	--	--	--	--	4.96	5.10	5.28	5.95	7.54	3.85
MnO	0.128	0.115	0.130	0.136	0.14	0.12	0.11	0.12	0.15	0.13
MgO	10.81	9.68	11.16	10.99	9.20	7.88	7.88	7.15	10.23	5.77
CaO	12.00	12.43	12.38	12.29	14.47	11.94	12.88	13.02	11.77	13.05
Na_2	2.42	2.63	2.20	2.20	2.43	2.93	2.94	2.83	2.51	2.55
K_2O	0.13	0.08	0.02	0.00	0.05	0.08	0.08	0.11	0.13	0.07
P_2O_5	0.00	0.02	0.01	0.01	0.03	0.03	0.03	0.02	0.07	0.02
LOI	1.63	1.03	0.99	1.52	--	--	--	--	--	--
Total	100.26	100.09	99.72	99.93	99.00	99.98	100.54	99.25	97.74	96.27
Sc	31	29	33	34	--	20	20	28	29	21
V	129	115	106	114	166	98	110	171	185	124
Cr	249	163	260	170	--	122	122	157	410	503
Co	51	46	44	43	--	39	--	37	47	26
Ni	132	119	109	117	--	106	106	92	230	108
Cu	246	184	160	143	--	90	90	101	--	37
Zn	59	71	42	42	--	61	61	53	--	48
Ga	14	14	11	11	--	--	--	--	--	
Ge	1.6	1.6	1.1	1.0	--	--	--	--	--	
As	8	n.d.	n.d.	n.d.	--	--	--	--	--	0.3
Rb	1	n.d.	n.d.	n.d.	--	--	--	--	--	3
Sr	175	173	151	152	162	199	197	190	115	188
Y	7.7	7.5	6.3	7.6	8	2	2	5	21	11.8
Zr	12	14	7	7	31	28	26	26	59	29
Nb	2.0	1.1	n.d.	n.d.	--	--	--	--	--	1.6
Ag	n.d.	n.d.	5.4	n.d.	--	--	--	--	--	
Sn	n.d.	n.d.	2	3	--	--	--	--	--	
Sb	n.d.	n.d.	n.d.	n.d.	--	0.03	--	0.039	0.04	
Cs	n.d.	n.d.	n.d.	n.d.	--	0.02	--	0.02	0.07	0.2
Ba	51	37	18	25	26	23	23	24	17	44
La	0.89	0.82	0.67	0.66	--	0.07	--	0.71	1.25	1.80
Ce	2.25	2.05	1.71	1.84	--	2.6	--	2	5.3	3.78
Pr	0.36	0.34	0.26	0.28	--	--	--	--	--	0.76
Nd	2.06	2.04	1.52	1.68	--	--	--	--	--	4.40
Sm	0.83	0.81	0.63	0.75	--	--	--	--	--	1.52
Eu	0.585	0.563	0.447	0.489	--	0.59	--	0.59	0.81	0.624
Gd	1.16	1.13	0.88	1.02	--	--	--	--	--	1.85
Tb	0.21	0.21	0.17	0.20	--	0.12	--	0.16	0.47	0.32
Dy	1.36	1.34	1.15	1.37	--	--	--	--	--	2.11
Ho	0.28	0.28	0.24	0.28	--	--	--	--	--	0.42
Er	0.84	0.84	0.71	0.83	--	--	--	--	--	1.16
Tm	0.118	0.116	0.102	0.118	--	--	--	--	--	0.178
Yb	0.73	0.73	0.62	0.71	--	--	--	--	--	1.07
Lu	0.107	0.108	0.089	0.104	--	--	--	--	--	0.157
Hf	0.6	0.4	0.3	0.3	--	0.23	--	0.3	1.28	0.88
Ta	n.d.	n.d.	0.02	n.d.	--	0.036	--	0.082	0.11	0.11
Tl	0.11	n.d.	0.12	0.10	--	--	--	--	--	0.03

Pb	n.d.	n.d.	n.d.	n.d.	--	--	--	--	--	0.22
Th	n.d.	n.d.	0.10	n.d.	--	0.016	--	0.019	0.15	0.31
U	0.03	0.03	0.03	n.d.	--	0.05	--	--	--	0.02
$Mg^{\#}$	76.89	76.81	76.97	76.11	78.60	75.37	74.72	70.41	72.87	74.83

Table 2

Sample		$^{143}Nd/^{144}Nd$	2σ	$^{87}Sr/^{86}Sr$	2σ	$^{206}Pb/^{204}Pb$	2σ	$^{207}Pb/^{204}Pb$	2σ	$^{208}Pb/^{204}Pb$	2σ
Brothers gabbros, 26° 19.1' N – 34° 50.5' E, † re-run, * duplicate											
B14-5-7	WR	0.513067	0.000010	0.703087	0.000007	18.7358	0.0021	15.5635	0.0021	38.4666	0.0063
†B14-5-7	WR					18.7309	0.0021	15.5575	0.0021	38.4468	0.0063
B14-5-7A	WR	0.513059	0.000007	0.703019	0.000007	18.6993	0.0030	15.5625	0.0027	38.4219	0.0075
†B14-5-7A	WR					18.7049	0.0027	15.5722	0.0024	38.4511	0.0068
B14-5-7B	WR	0.513057	0.000010	0.703049	0.000007	18.6391	0.0015	15.5667	0.0014	38.4150	0.0038
†B14-5-7B	WR					18.6277	0.0016	15.5605	0.0016	38.3880	0.0048
B14-5-8	WR	0.513062	0.000010	0.702977	0.000008	18.6679	0.0009	15.5660	0.0008	38.4764	0.0021
†B14-5-8	WR					18.6669	0.0009	15.5647	0.0008	38.4724	0.0021
BRO-28	cpx	0.512990	0.000010	0.703526	0.000008	18.9007	0.0073	15.5483	0.0060	38.3809	0.0158
*BRO-28	cpx	0.512972	0.000015	0.703538	0.000025						
†BRO-28	cpx			0.703528	0.000034						
BRO-A	cpx	0.513074	0.000008	0.703396	0.000008						

BRO-B	cpx	0.513083	0.000008	0.703457	0.000008	18.6434	0.0069	15.5621	0.0056	38.2702	0.0136
*BRO-B	cpx	0.513080	0.000019								
Sample		**$^{143}Nd/^{144}Nd$**	**2σ**	**$^{87}Sr/^{86}Sr$**	**2σ**	**$^{147}Sm/^{144}Nd$**					
QUSEIR B1-X gabbros, 25° 40.488' N – 35° 09.137' E, † re-run, * duplicate.											
Qs_WR3	WR	0.513061	0.000009	0.704339	0.000010	0.215279					
†Qs_WR4	WR	0.513070	0.000017	0.704405	0.000008	0.212996					
*Qs_WR4	WR			0.704406	0.000008						
Qs_cpx	cpx	0.513078	0.000018	0.705110	0.000006	0.294399					
†Qs_cpx	cpx			0.705090	0.000007						
Qs_plg	plg	0.513056	0.000034	0.703457	0.000006	0.132961					

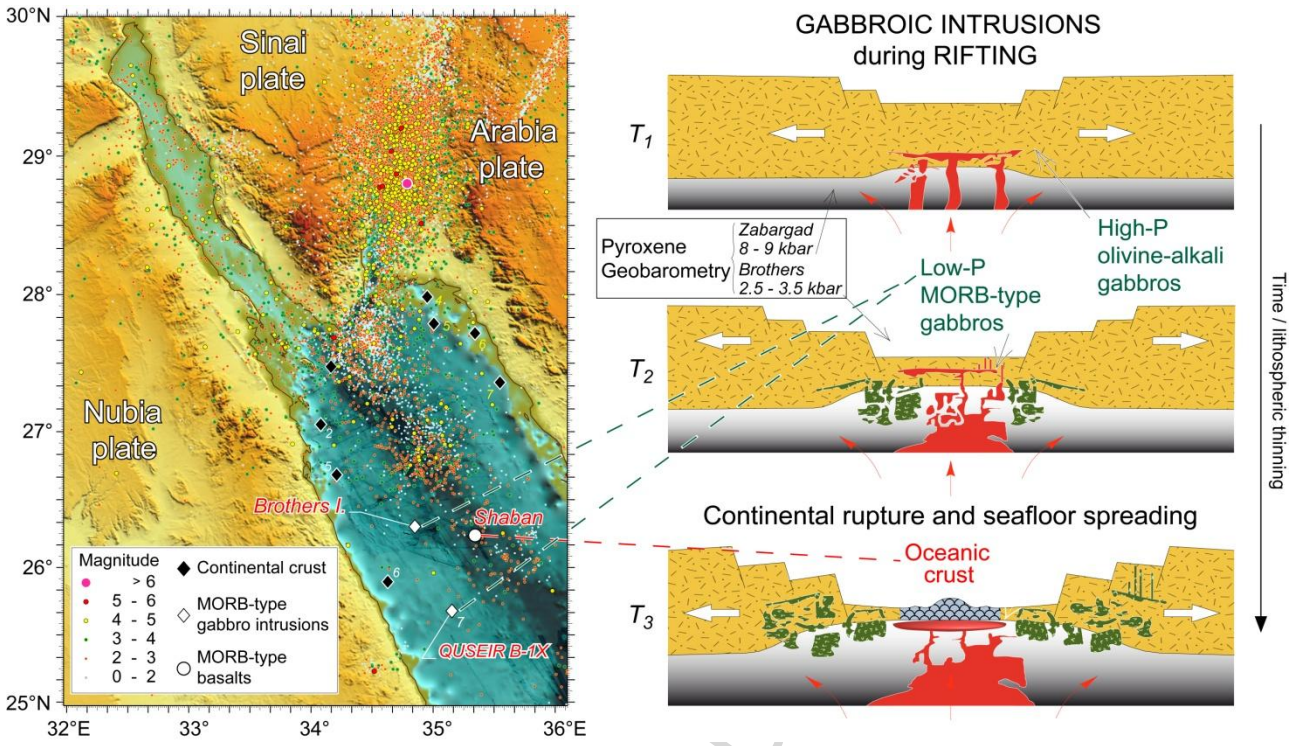

Graphical abstract